

Biomimetic Skins Enable Strain-Perception-Strengthening Soft Morphing

Peng Xiao, Wei Zhou, Yun Liang, Shiao-Wei Kuo, Qing Yang, and Tao Chen*

Biological soft tissues are typically characterized of strain mechanical stiffening for injury prevention, yet the capability to achieve active awareness via perception strengthening still remains a challenge. However, creatures have projected their 2D or 3D deformation in a safe way via perception regulation. In this work, strain-perception-strengthening (SPS) enabled soft skins that allow the dynamic transformation from tactile to pain-sensing are proposed. The synthetic skin featured with elastic, conductive, and adaptive properties is composed of elastomeric thin-film and assembled graphene nanosheets with an interlocked structural interface. In the SPS-enabled sensory system, the strain-perception-threshold value can be regulated from $\approx 7.2\%$ to $\approx 95.3\%$. The integrated skin-like system can effectively imitate the normal tactile and pain feeling of soft tissues (e.g., unidirectional stretching of muscle tendon and irregular stretching deformation of hand skin). Furthermore, inspired by the pufferfish, a bionic pufferfish with synthetic skin is designed, enabling it to sensitively capture the external mechanical stimuli such as tiny airflow and finger touch, and further inflate itself to a 3D deformation determined by the SPS effect. The concept of soft skins with SPS effect demonstrates potential fields in safe human-machine interaction, smart prosthetics and soft robotics.

moldable elastomers with strain mechanical stiffening through the self-assembly of linear-bottlebrush-linear triblock copolymers, allowing the typical imitation of tissue-like mechanical characteristics.^[10]

Beyond the mechanics of the materials, certain tissues of creatures such as vertebrates have the capabilities to actively perceive the mechanical stimuli that may cause injury, and further rapidly react to prevent dangers.^[11–13] These tissues, coupled with somatosensory systems, can experience a regulated sensory threshold transition from tactile to pain-sensing. In the creatures' sensory systems, tactile receptors are responsible for the discriminative touch and non-harmful stimuli.^[14] Nociceptors that depend on locality and modality are also considered to be important and indispensable, which can deliver danger signals to brains for risk management.^[15–17] Therefore, prior to strain mechanical stiffening, the active protection requires intense and rapid


1. Introduction

In biological systems, soft tissues can effectively regulate their mechanical strength via strain stiffening to avoid injury, in which the elastic moduli increase rapidly and sharply under a narrow strain range.^[1] Specifically, the mechanical adaptation arises from their intrinsic composite structures based on the mechanics of natural materials.^[2] The passive mechanical defense has inspired the synthesis of biomimetic materials with tissue-like mechanics.^[3–9] For example, Sheiko et al. designed

pain warning triggered by the sensory system. Although the conventional electronic skin systems can simulate the human tactile functions or pain ones via the predetermined threshold of resistance change,^[18–22] few synthetic soft skins focus on dedicated capabilities for strain perception strengthening (SPS) with a similar trend as the strain mechanical stiffening.^[23] In the SPS-enabled strain-responsive system, the gauge factor (GF) (the first derivative of the normalized resistance versus strain) can experience a positive correlation with the applied strain. When the strain value is lower than the threshold, the

P. Xiao, W. Zhou, Y. Liang, T. Chen
Key Laboratory of Marine Materials and Related Technologies
Zhejiang Key Laboratory of Marine Materials
and Protective Technologies
Ningbo Institute of Materials Technology and Engineering
Chinese Academy of Sciences
Ningbo 315201, China
E-mail: tao.chen@nimte.ac.cn
P. Xiao, W. Zhou, Y. Liang, T. Chen
School of Chemical Sciences
University of Chinese Academy of Sciences
Beijing 100049, China

S.-W. Kuo
Department of Material and Optoelectronic Science
Center of Crystal Research
National Sun Yat-Sen University
Kaohsiung 804, Taiwan
Q. Yang
State Key Laboratory of Modern Optical Instrumentation
College of Optical Science and Engineering
International Research Center for Advanced Photonics
Zhejiang University
Hangzhou 310027, China
Q. Yang
Research Center for Intelligent Sensing
Zhejiang Lab
Hangzhou 311100, China

 The ORCID identification number(s) for the author(s) of this article can be found under <https://doi.org/10.1002/adfm.202201812>.

DOI: 10.1002/adfm.202201812

GF value increases slowly, which corresponds well to the tactile sensing of creatures' sensory system. Once the strain that is higher than the threshold value is applied, the GF value can experience a sharp increase under the same strain increment. The fast change of the GF value under unit strain can be considered as a reminder of pain-sensing. Note that this changing trend is similar to the function of nerve endings, which provides a warning signal for mechanical strain danger. Therefore, the SPS-based sensory skin can respond sharply to the strain threshold for remarkable improvement of GF value, allowing the perception transition from tactile to pain-sensing. More importantly, the exploration of SPS materials systems that are independent of physical size, shape and initial conductivity will inspire the development of self-regulated sensors and integrated soft robots for risk control of human-machine interfaces.

We demonstrate a SPS-effect enabled ultra-thin skin (elastic and conductive film [ECF]), formed by the interface interlocked structure of assembled 2D nanomaterials and thin elastomers interacting on the water surface. Here, graphene nanosheet is used as a 2D model due to its layered topology, excellent conductivity and uniform assembled structure. Unlike the 1D nanotubes-based ECFs, the 2D-based ones demonstrate a positive correlation between GF and strain, which is analogous to the sensory systems of vertebrate creatures. They can form a dynamic sensing network that responds sensitively to low strain stimuli for normal sensing and also reacts to strain threshold with several orders of magnitude enhancement in normalized resistance for pain-sensing. Specifically, the strain threshold can be effectively regulated from $\approx 7.2\%$ to $\approx 95.3\%$, which can contribute to the development of diverse SPS-related applications, such as smart muscle tendon under uniaxial stretch, and artificial hand skin under pinch and stretch. Furthermore, inspired by the pufferfish, a smart fish model featured with a morphable and perceptible belly was designed to sensitively perceive tactile signals of tiny airflow, mechanical touch and further be actuated to a bulged shape with 3D deformation detection and pain warning under strain threshold. This proposed SPS concept is expected to provide an alternative and effective pathway for self-regulated soft robotics and safe human-machine interacted interfaces.

2. Results and Discussion

2.1. Strain-Perception-Strengthening Enabled by Assembled Graphene-Based ECF

In nature, creature's skins have evolved into rich diversity. As the first protective barrier, skins are further endowed with unique capabilities of perception and desirable deformation to adapt to the changeable environment. Specifically, compared with conventional synthetic materials, a typical characteristic of soft tissue (e.g., skin) is mechanical strain induced skin stiffening (passive protection) to prevent injury.^[1] However, these tissues are also endowed with sensory systems to achieve active protection. For example, human skin can sensitively capture the mechanical stimuli of typical stretching strain, and further distinguish them into specific signals, such as tactile and

pain-sensing (Figure 1A). For the real skin, tactile corpuscles and nociceptive endings located in the dermis layer are responsible for tactile and pain-sensing, respectively. When a gentle mechanical force is applied to the skin, the tactile receptors can rapidly respond and further convert it into a normal tactile signal. Further increased force (e.g., hard pinch, high stretch) that may induce uncomfortable feelings will be captured by the nociceptive endings (Figure 1B). In our system, an artificial skin featured with thin, deformable and perceptive properties was designed and further transferred onto a hand model surface for mechanical sensing. We observe that it can be easily stretched, followed by the formation of wrinkles (Figure 1C). Here, the artificial skin composed of a conductive graphene layer and elastic Ecoflex layer can be fabricated at the air/water interface on a large scale and easily transferred onto diverse substrates. Similar to the human skin, the artificial skin on the water surface can be readily touched, pinched and further stretched (Figure 1D).

Generally, creatures with compliant soft tissues can respond to the overstretched strain via a typical mechanical stiffening to prevent potential injury. Note that collagen is widely distributed in the tissues of mammals. The mechanical stress-strain characteristics of the collagen are featured with a specific shape like "J", which is also defined as mechanical strain-adaptive stiffening.^[24–26] Therefore, the strain-adaptive mechanical stiffening phenomenon exists in most of the mammals. Here, the tissue of pig skin was alternatively acquired to test the mechanical behavior, demonstrating a specific strain mechanical stiffening (Figure 1E). Note that the achieved mechanical strength can experience a fast increase under the strain threshold (Figure S1, Supporting Information). The mechanical stiffening aims to generate considerable strength to avoid injury. However, the effective perception of danger signals is expected to be more important for the realization of active protection. The mechanical strain stiffening has also inspired us to develop an electrical perception strengthening system that we refer to as the SPS effect. In the SPS-based materials, the normalized resistance can experience a typical "J"-like changing trend under the applied strain, which can function as the strain-responsive pain sensor to actively perceive the overstretching behavior (Figure S1, Supporting Information). Owing to the introduction of the graphene nanosheet layer, the elastic membrane was further endowed with the capability of perception to external mechanical stimuli. As displayed in Figure 1F, when the applied strain reached a certain stretched threshold, the normalized resistance represented a strain perception strengthening effect. The phenomenon is similar to the sensory system of humans, which can simultaneously capture the tiny and sharp mechanical force, and further distinguish and name them. In the artificial skin system, the whole curve can be divided into two parts, including the tactile sensing before the threshold and pain ones after the threshold (Figure S2, Supporting Information). It is noted that analogous to the skin perception system, the slope of normalized resistance also experiences an increasing tendency to the increased strain. In our work, the potential working mechanism was schematically illustrated in Figure 1G. In the stretching process, the low strain just leads to the relative sliding of graphene nanosheets with contacted states. Furthermore, higher strain allows remarkable separation

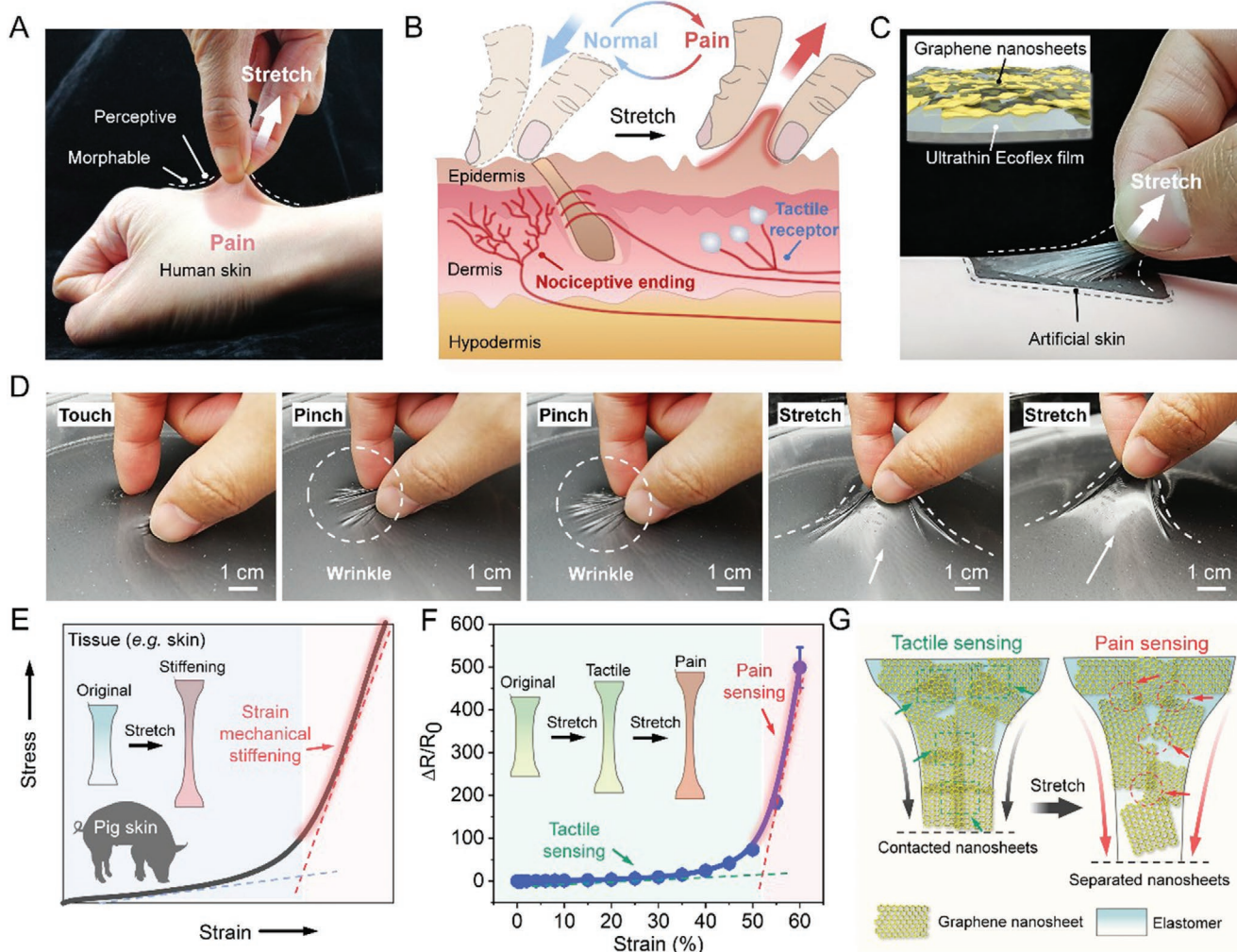


Figure 1. Bioinspired artificial skins composed of ultrathin and conductive films enabling strain-perception-strengthening effect for sensing regulation. A) Photo of a real hand skin that is highly stretched with a pain feeling. B) Schematic illustration of skin morphology with fingers touched and stretched state, showing tactile and pain feeling. C) An artificial skin attached onto a hand model surface is easily stretched, showing remarkable skin-like wrinkles. D) Photos of ECF at air/water interface that is touched, pinched and stretched with good artificial skin behaviors. E) A schematic of soft tissue's stress-strain curve (pig skin was used here), showing the mechanical response of intense strain stiffening behavior. F) The normalized resistance versus applied strain curve in a uniaxially stretched state, demonstrating a tendency of strain strengthening of the normalized resistance (the sample size: $5\text{ cm} \times 5\text{ mm}$, test number $n = 5$). G) The potential micro-scale mechanism of transition from tactile to pain-sensing.

of nanosheets, resulting in a sharp decrease of the normalized resistance.

2.2. Construction and Characterization of ECF

To construct a biomimetic skin with thin, elastic and conductive features, a fabrication strategy based on a liquid substrate is achieved in Figure S3, Supporting Information. The mechanically exfoliated graphene nanosheets with an average thickness of about 2.4 nm were assembled into a closely packed film on the water surface enabled by the Marangoni effect and capillary force driving compression (Figure 2A and Figure S4, Supporting Information).^[27,28] Based on the interface functionalization strategy,^[29] the water supported graphene film can be further functionalized by elastomer to achieve an ECF, of which

the graphene nanosheets were partially embedded into an elastic matrix with good structural stability. In our system, the graphene film was assembled on the water surface and partially wetted by water molecules. Once the elastomeric precursor in heptane solution was applied onto its surface, the air side of the graphene film could be covered by the polymer solution. After in situ curing process, the water side of the film was protected by water phase, resulting in the partially embedded graphene nanosheets into the elastomer matrix. As shown in Figure 2B, the as-prepared ECF could be easily lifted from the water surface. The schematic in Figure 2C illustrates that graphene nanosheets were partially embedded into the elastomer matrix with favorable conductivity. Prior to elastomer functionalization, a scanning electron microscopy (SEM) image of assembled graphene film was characterized, showing a close-packed laminated structure (Figure 2D). After interfacial functionalization,

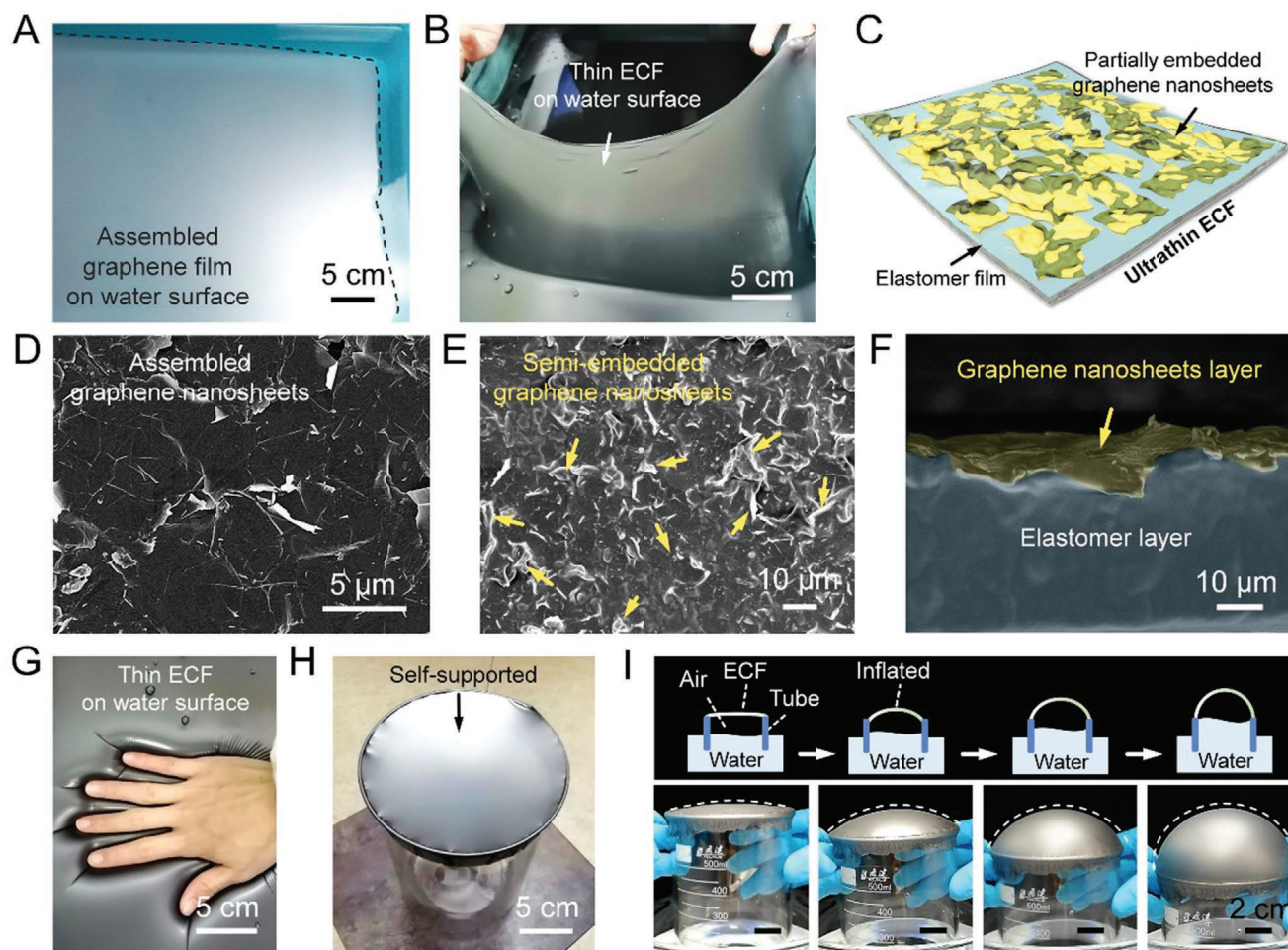


Figure 2. ECF fabrication and structural characterization. A) Photo of assembled graphene nanosheets on large scale on the water surface. B) Photo of large-area ECF fabricated at air/water interface, which can be easily transferred from the water surface. C) Schematic of thin ECF composed of partially embedded graphene nanosheets and elastic elastomer layer. D) SEM images of assembled graphene film, ECF: E) surface morphology of graphene side and F) cross-section with bilayer structure. G) ECF on water touched with fingers, showing highly compliant feature. H) ECF attached to beaker for a self-supported one. I) ECF was easily actuated by air pressure.

an interlocked structural interface was formed (Figure 2E and Figure S5, Supporting Information). SEM cross-sectional image further confirmed the layered structures in ECF (Figure 2F). In addition, 2D mapping of the Raman spectrum of the ECF was also investigated in Figure S6, Supporting Information, demonstrating a remarkable color difference of characteristic G peak in ECF.

In our system, the molecular-level water surface enabled the formation of thin, uniform and easy-transferrable ECF due to the Marangoni effect. The gentle touch of the fingers resulted in compliant adaption and wrinkled geometry of the ECF (Figure 2G). Furthermore, it could be conformally transferred onto the non-planar surface and further employed as a self-supported film, which was easily actuated to 3D morphing via the pressured air (Figure 2H,I). Analogous to creatures' skins, the ECF was endowed with highly conformal characteristics, and could spread smoothly along the hierarchical surface of natural skins (Figure S7, Supporting Information). To measure the electric stability of the cyclic stretching, varied strain ranging from 0.1% to 30% was loaded on the ECF-based sensor. It shows a

reversible resistance variation during the load and unload strain cycles (80 cycles) (Figure S8, Supporting Information). Besides, the sensor can also realize a real-time response and recovery to the dynamic mechanical strain with a wide range of frequencies ranging from 0.01 to 1 (Figure S9, Supporting Information). Although the graphene-elastomer composite films have been widely studied to construct strain sensors, compared with the previous research, the interface strategy enabled ECF can be endowed with an ultra-thin thickness (about 32 μm) and higher GF value (higher than 7500). Superior to the conventional composite film fabricated on solid substrates, our ECF fabricated on the water surface can not only effectively detect 2D deformation, but actively perceive the pneumatic 3D morphing behavior. Also, we summarized the recent works of graphene-elastomer-based strain sensors in Table S1, Supporting Information, in which the ECF represented typical features of thin thickness, high GF and self-perceptive 3D morphing. Moreover, we also conducted the hysteresis measurement of the graphene-Ecoflex system, which demonstrated a good overlapping during the stretched and released cycles under the strain of

lower than 25% (Figure S10, Supporting Information). Owing to the intrinsic 2D feature of the graphene layer, the ECF can effectively simulate and achieve the function of skin-like tactile and pain feeling. Note that the graphene nanosheets and elastomeric substrate can experience a shear strain for sheets sliding and normal strain for reversible deformation, individually.^[30] Based on this reason, to simplify the definition of the strain, the uniaxial stretching of the ECF is defined as the strain. As illustrated in Figure S11, Supporting Information, a simplified sketch of the working mechanism represents that the assembled graphene nanosheets experience face-to-face sliding at low strain, leading to a relatively slow increase of the contact resistance in the tactile sensing range. When the stretching strain further increased, the distance between adjacent sheets was remarkably widened. The sharp decrease of contact area among graphene nanosheets may result in the rapid increase of contact resistance of ECF for the pain-sensing area.

2.3. SPS Behavior Adjustment and Potential Mechanism

We further investigated the resistance change mechanism of 2D and 1D nanotubes based ECF strain sensors. As displayed in Figure 3A and Figure S2, Supporting Information, the normalized resistance versus strain curve of 2D-based ECF was divided into four stages by using the slope value, which was also defined as GF. As a result, it presents an ever-increasing GF with the value of 22 and 130 at the first and second stages, respectively. The changing trend of GF values showed a slow increase at low strain for tactile perception and a rapid increase at high strain for pain (Figure S12, Supporting Information). It is noted that the continuous increase of GF is analogous to sensory systems of creatures' skins that represent a positive relationship between sensing intensity and the applied mechanical force. To further investigate the reproducibility and stability of the 2D based ECF, a large-area ECF was fabricated on the water surface (Figure S13A, Supporting Information). And three samples were acquired from different parts of the ECF, demonstrating similar conductivity in the I-t curve (Figure S13B, Supporting Information). In addition, we also explored the normalized resistance versus strain curves of the three samples, showing an analogous SPS trend (Figure S13C, Supporting Information). The result illustrates that the interfacial functionalization method can be successfully scaled up, enabling favorable uniformity and repeatable electrical performance. However, compared with the 2D nanosheets, 1D-based nanomaterials, such as metal nanowires, are featured with a large length/diameter (L/D) ratio, demonstrating extensible applications in stretchable electronics.^[31–34] Moreover, for the 1D nanotubes-based ECF, the normalized resistance curves of multi-walled nanotubes (MWNT) and single-walled nanotube (SWNT)-based ECF both demonstrated the wide response range of the uniaxial strain of 450% and 600%, individually (Figure S14, Supporting Information). This may derive from the intrinsic high L/D ratio with slow change of the contacted resistance. Compared with the 2D-based ECF, the GF of 1D-based ECF at low strain range demonstrated prominently reduced values of 8.12, 2.25 and 1.71, 0.78, respectively, during the first two stages (Figure 3B,C, Supporting Information). The result indicates that there exists

a negative correlation between strain and GF values in the low strain range for 1D-based ECF sensors.

More importantly, it was found that the composite of graphene nanosheets and SWNT demonstrated either a 1D or 2D-based ECF-like GF changing trend, which could be effectively controlled by adjusting the weight ratio of the above-mentioned two nanomaterials. When higher content of SWNT (graphene/SWNT is 1:5 and 1:3) was applied, the entire ECF presented the GF characteristic of 1D-based ECF (Figure 3D). Further increasing the content of graphene (the weight ratio of graphene/SWNT is higher than 1) can remarkably transform the GF characteristic to that of 2D-based ECF (Figure 3E,F). Note that the appropriate introduction of 2D nanomaterials into 1D-based ECF can result in a positive correlation between GF and applied strain, which can be a favorable candidate for the realization of pain-sensing. In our experiment, we have adjusted the weight ratio of 2D graphene nanosheets and 1D SWNT for pain-sensing. As illustrated in Figure S15, Supporting Information, when the weight ratio of graphene in the 1D/2D composite is maintained at more than 0.5, the achieved ECF can represent the characteristics of 2D-based ECF. Therefore, for the samples of S1G1, S1G3, and S1G5, the pain strain threshold could reach up to $\approx 116\%$, $\approx 95\%$, and $\approx 52\%$, respectively. The result demonstrates that the pain strain threshold can be effectively controlled via the controllable hybrid of 1D and 2D nanomaterials. In the biomimetic sensing system, an adjustable strain threshold is highly desired for the adaption to diverse application. In our system, the controllable combination of 1D and 2D nanomaterials can enable adjustable pain strain threshold to meet diverse demands. As a result, a skin-like sensing performance can also be effectively simulated and further adjusted using the composite system. In our work, a simplified sketch of a potential working mechanism is schematically illustrated in Figure 3G. For the 1D-based ECF, when the uniaxial stretch is applied, randomly entangled nanotubes fixed in the elastic polymer may firstly experience rapid displacement, followed by a quick increase of contact resistance. Further applied strain may straighten the bent nanotubes, in which process the contact points/areas and resultant contact resistance among nanotubes change slowly. As a result, GF values firstly increase and then decrease with the increase of applied strain. However, for the 2D-based ECF, the graphene nanosheets with a low L/D ratio experience a face-to-face sliding with a slow decrease of contacted areas at low strain and severe separation with a sharp decrease of contacted areas at higher strain. For the potential mechanism of the SPS effect, SEM characterization was conducted to further investigate the surface morphology under the uniaxial strain. In order to clearly observe the morphology information, assembled graphene nanosheets were directly transferred onto the elastomer surface for the ECF. As shown in Figure S16, Supporting Information, it was found that with the increase of uniaxial strain, the cracks of assembled graphene nanosheets showed a gradually increased tendency. More importantly, a higher strain may cause larger cracks generation and severely reduced conductive pathways. In addition, finite element simulation and analysis (FEA) enabled by the COMSOL Multiphysics software was also conducted to simulate the changing process of the normalized resistance under the stretched strain (Figure S17, Supporting

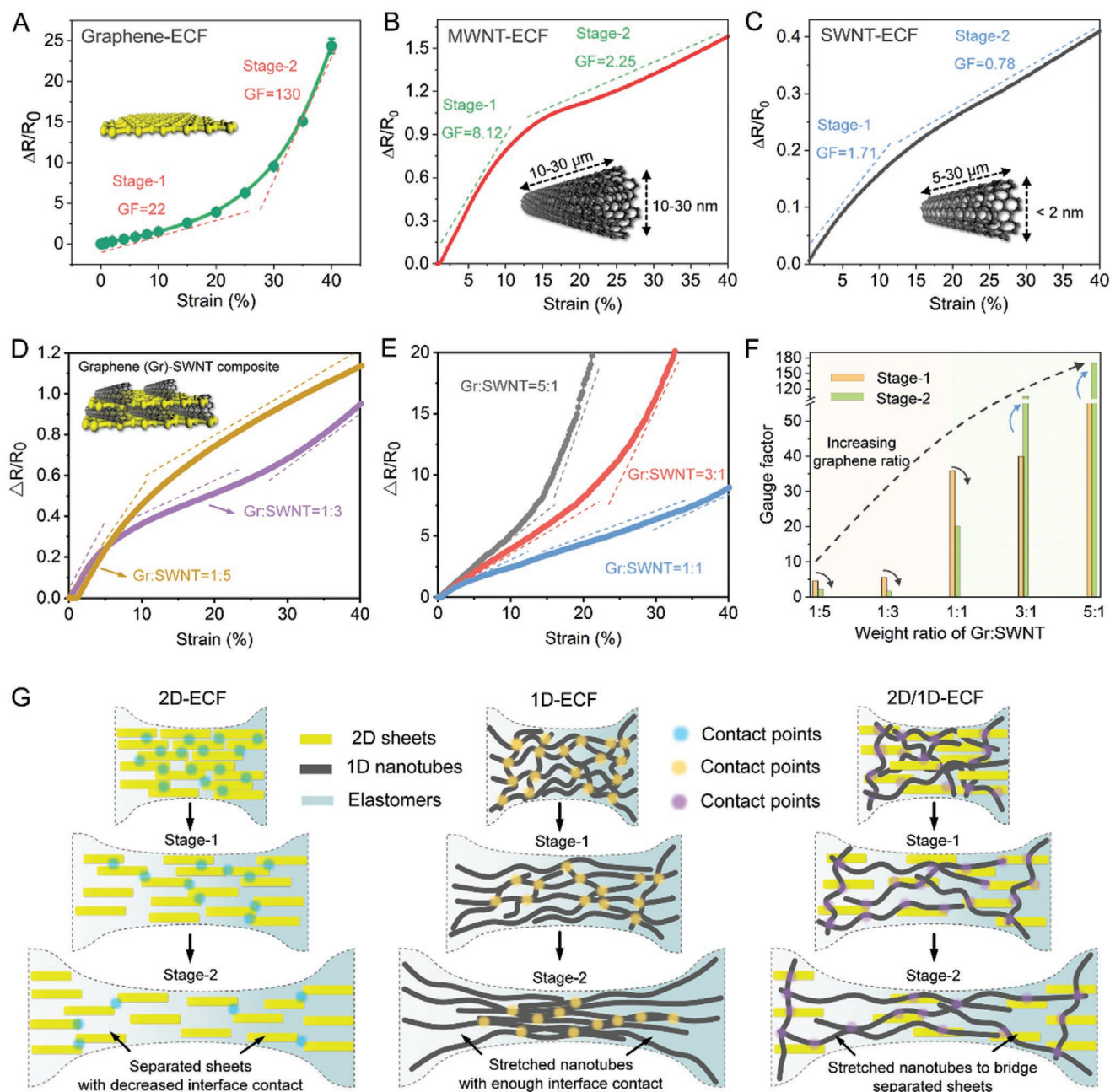


Figure 3. The control of SPS performance and its mechanism. A) The normalized resistance versus curve of graphene-based ECF with ever-increasing GF within two stages. B-C) The normalized resistance versus strain curves of MWNT and SWNT-based ECF, representing decreased GF in the second stage. D-F) The composites of graphene and SWNT with a series of weight ratios demonstrate adjustable GF (all the sample size: $\approx 5 \text{ cm} \times 5 \text{ mm}$, test number: $n = 5$). G) Schematic illustration of the working mechanism of a series of ECF derived from 1D, 2D and 1D/2D composite nanomaterials under the increased strain.

Information). In the simulation analysis, graphene nanosheets (six nanosheets as one layer) were directly attached onto the elastomer surface with a series of layers. With the increase of applied strain, the surface stress and surface potential were simulated and collected. When the uniaxial strain reached the threshold value, the calculated normalized resistance demonstrated a sharp increase with a “J” like shape, which was similar to the experimental result (Figure S18, Supporting

Information). Figure S19, Supporting Information clearly indicated that there was an apparent difference in the changing tendency of GF between 1D and 2D-based ECF at low strain (samples with 40% strain). Besides, the introduction of high-content nanotubes into 2D-based ECF can prominently bridge the separated gaps between graphene nanosheets to effectively decrease the contact resistance for the controllable transformation of GF changing trend. Therefore, the effective balance

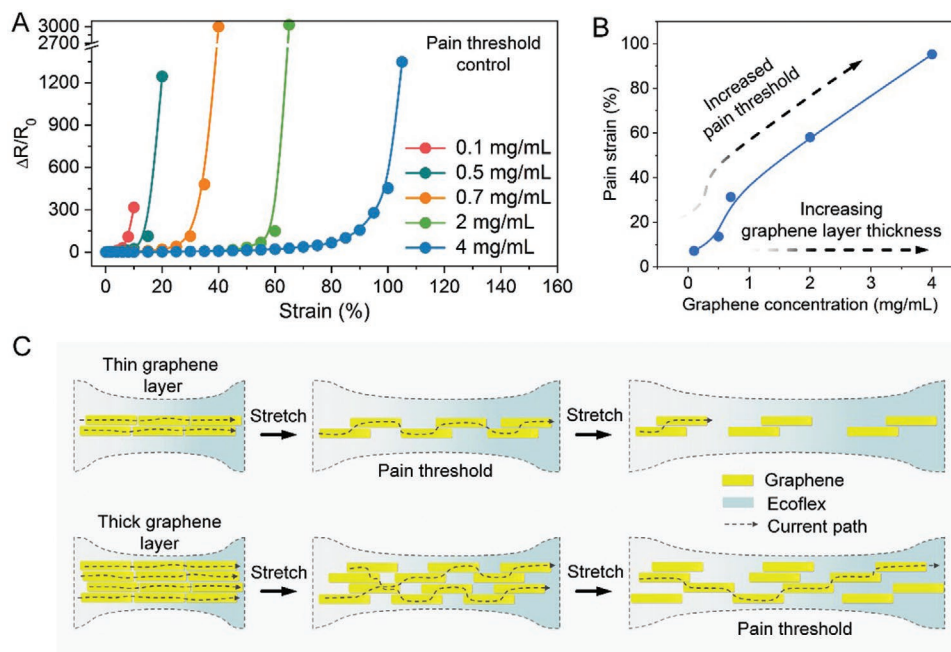


Figure 4. The threshold control and mechanism of assembled graphene-based ECF. A) The normalized resistance versus strain curves, in which the pain threshold can be effectively controlled through the graphene layer thickness enabled by changing graphene suspension concentration (the sample sizes: $\approx 5 \text{ cm} \times 5 \text{ mm}$). B) Pain threshold strain versus graphene suspension concentration curve (test number, $n = 5$). C) Schematic illustration of the working mechanism of ECF with different graphene layer thickness, demonstrating an adjusted pain threshold.

of 1D nanotubes and 2D nanosheets can lead to controllable sensing performance for specific electronic applications.

2.4. SPS Threshold Control of Graphene-Based ECF and its Mechanism

In creatures' sensory system, the pain threshold may vary with different parts of skins/tissues, or different individuals in the same part. Therefore, an effective control of the pain threshold is considered to be significant in the biomimetic skins. Based on this, the approach of pain threshold control was explored in our system. As shown in **Figure 4A**, the strain threshold can be effectively adjusted ranging from $\approx 7.2\%$ to $\approx 95.3\%$ by changing the concentration of graphene sheets. The concentration of graphene nanosheets from 0.1 to 4 mg mL^{-1} enabled the formation of a controllable thickness of assembled graphene films. Note that higher concentration ($>4 \text{ mg mL}^{-1}$) can be not adopted in our experiment due to the poor graphene dispersion in ethanol solvent. As a result, there is a positive relationship between pain strain threshold and graphene nanosheets concentration (**Figure 4B**). In addition, the potential control mechanism shown in **Figure 4C** illustrates that the assembled graphene film with thinner thickness may lead to the formation of separated nanosheets at low uniaxial strain. Further increasing the thickness of graphene layers can effectively expand the conductive path and transform the pain strain threshold to a higher value. Furthermore, the control mechanism of the strain threshold was also simulated in FEA, in which 2, 4, and 6 layers of graphene nanosheets were applied to simulate the trend of the threshold control. As displayed in

Figure S18, Supporting Information, with the increase of graphene layers, the calculated strain threshold could move to a higher value, demonstrating a positive correlation between layer numbers and strain threshold. The simulated result further confirmed the feasibility of threshold control. The graphene layer thickness-dependent strain threshold is expected to show significant potential in the wide-range simulation of natural creatures' sensory systems.

2.5. 3D Morphing and their SPS Performance

Owing to the ultra-thin and adaptive feature of ECF, it can also function as a self-supported one for a circumferential 2D shape and be further inflated to realize a stretch for 3D displacement. The resulted 2D to 3D transformation, similar to the skin behavior of creatures (e.g., air-blowing of pufferfish, bulging of frog sound-sac), can be inflated to a series of states from flat to highly stretchable near-sphere form.^[29,35] Inspired by the natural phenomenon, the shape-morphing behaviors of 3D shapes are highly explored and are of significant interest for a variety of soft robotics.^[36,37] Specifically, for the pneumatic or hydraulic systems, the effective control of actuation is highly important to determine the actuated degree and avoid the potential breakage. Similar to self-perceptive 2D morphing, the introduction of sensing function into the 3D morphing system can effectively regulate the actuation behavior. The achieved ECF can effectively adapt to the targeted surfaces for supported mechanical sensing under 2D morphing. More interestingly, superior to conventional supported devices, it was further employed to function as a self-supported sensor for effective 3D morphing

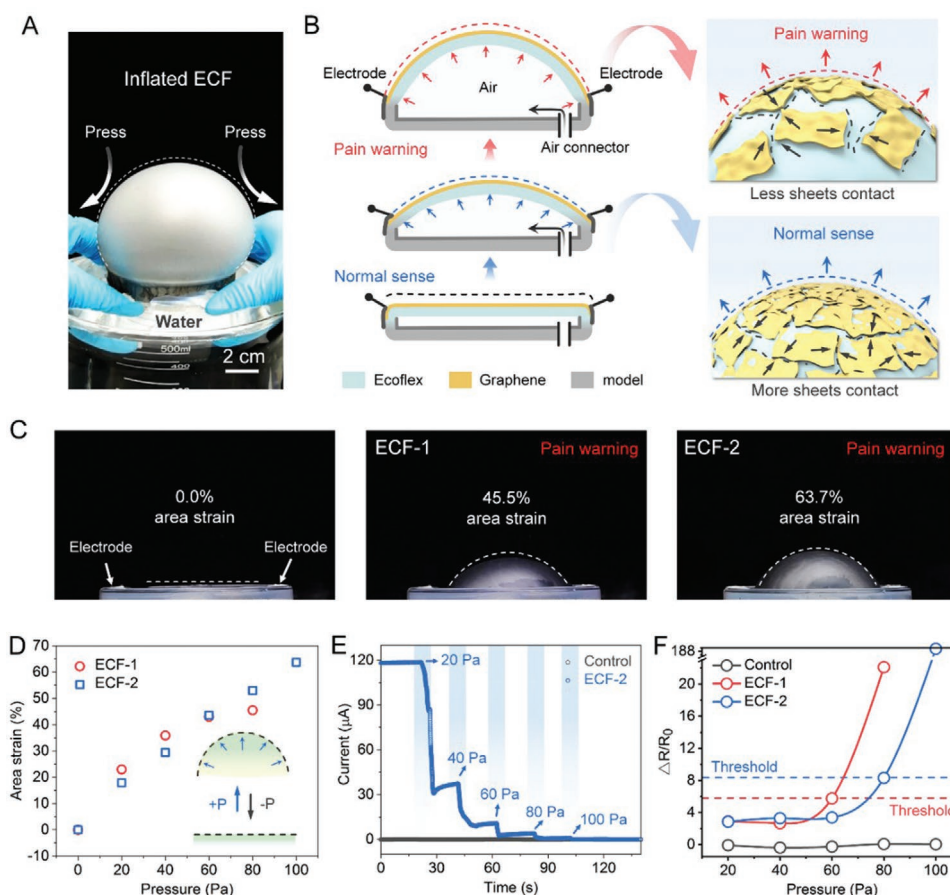


Figure 5. 3D pneumatic actuation and SPS enabled morphing regulation. A) Photo of ECF attached to container surface for a self-supported one, which can be easily inflated into a bulging state driven by gently pressing it into water. B) Schematic illustration of ECF-based integrated actuator pneumatically driven by low pressure, and the 3D deformation stages can be sensitively monitored, including the tactile and pain-sensing state. C) Photos of ECF-based actuators that experience specific 3D actuation behaviors, and the pain strain can be effectively adjusted (the diameter of the self-supported circular film: ≈ 4 cm). D) Area strain versus actuated pressure under applied pressure lower than 100 Pa (test number, $n = 5$). E) Current versus time curves in the pneumatic actuation process. F) The normalized resistance versus applied pressure curves in 3D actuation, in which the pain threshold can be controlled (test number, $n = 5$).

sensing (Figure S20, Supporting Information). In addition, the hydraulic actuator based on ECF was also constructed with high stability and load. As displayed in Figure S21, Supporting Information, the introduction of water medium endowed the actuator with prominent improvement of loading capability (more than one thousand times weight heavier than itself). Further combination of programmable rigid templates could enable 3D morphing, such as a face with various shapes of organs and succulent plants (Figure S22A,B, Supporting Information). Even hierarchical geometries of Chinese words could be also dynamically displayed, demonstrating significant potential in the design of biomimetic models and their applications (Figure S22C, Supporting Information). Specifically, owing to the thin feature of the ECF, it could be conformally attached to the edge of a tube for a self-supported one. When it was gently pressed into water. A 3D deformation driven by air pressure inside the tube was easily realized even without any pneumatic devices (Figure 5A). In our device, the ECF integrated with electrodes was adaptively adhered onto a model with air pump for a sealed device, which could be pumped to a certain 3D shape

with the tactile and pain-sensing function (Figure 5B). Note that compared with the uniaxial strain, the inflated 3D shape with circumferential strain prominently increased the contact resistance from the circumferential direction. Here, we use area strain that is defined as the relative area change to define the degree of 3D stretching strain.

To measure the possibility of the self-perceptive 3D actuation, an inflatable model with a hollow circle was designed and further integrated with ECF and electrodes (Figure 5C). Analogous to the uniaxial stretch, the 3D inflation also demonstrated the pain-sensing function under the stretched area strain. Compared with the pure elastomer films, the ECF-enabled pneumatic actuator resulted in remarkable change of current signal and represented good repeatability under cyclic stretching strain (Figures S23 and S24, Supporting Information). In our system, the pain threshold of 3D actuation was controlled by adjusting the concentration of graphene suspensions, demonstrating the area strain threshold of 45.5% for ECF-1 (graphene concentration of 2 mg mL^{-1}) and 63.7% (graphene concentration of 4 mg mL^{-1}) for ECF-2, respectively. Owing to the thin feature of ECF, it can be

easily inflated with low pressure (lower than 100 Pa) for high area strain (Figure 5D). The low energy consumption can effectively simplify the device and reduce the potential risk of explosion induced by high pressure. To detect the electrical signal during the 3D actuation, the real-time current versus time curves of ECF-2 and control (pure Ecoflex film) samples were investigated in Figure 5E. With the increase of pumped air pressure from 20 to 100 Pa, the corresponding current of ECF-2 presented a step-by-step decrease. The normalized resistance versus air pressure curves illustrated that compared with the control sample, the normalized resistance of ECF-1 and ECF-2 both demonstrated remarkable strain strengthening effects at a certain pressure threshold. Specifically, the pumped pressure of pain threshold for ECF-2 was higher than that of ECF-1 (Figure 5F).

2.6. Soft Tactile and Pain-sensing using SPS Principle

Creatures' skin can adapt itself to a certain deformation state controlled by the tactile and pain perception. Our ECF-based

mechanical sensor (ECF with graphene concentration of 0.5 mg mL^{-1}) was further employed to function as an artificial muscle tendon. As shown in **Figure 6A**, a skeleton model with movable joints was selected and integrated with the artificial muscle tendon. When the ankle was bent to different states under the uniaxial strain (5.7%, 12.2%, 14.9%, 19.2%, and 25.0%), the ECF-based sensor could sensitively perceive the varied bending angles (Figure 6B). When the uniaxial strain reached a threshold value, the remarkable improvement of GF (value from ≈ 22 to ≈ 358.2) could give suggestive information of pain warning (Figure 6C). Specifically, a visual display could be achieved via nonlinear fitting of the exponential function, subsequent linear fitting of two lines at different stages of the "J" shape curve, and final intersection calculation of the two linear equations for pain-strain color mapping (In the Supporting Information). Therefore, the red color of strain values can remarkably remind the potential pain warning. In addition, the applied area strain out of the planar surface was also imposed on the ECF sensor to simulate the behavior of skin stretching. Figure 6D showed that the ECF with graphene concentration

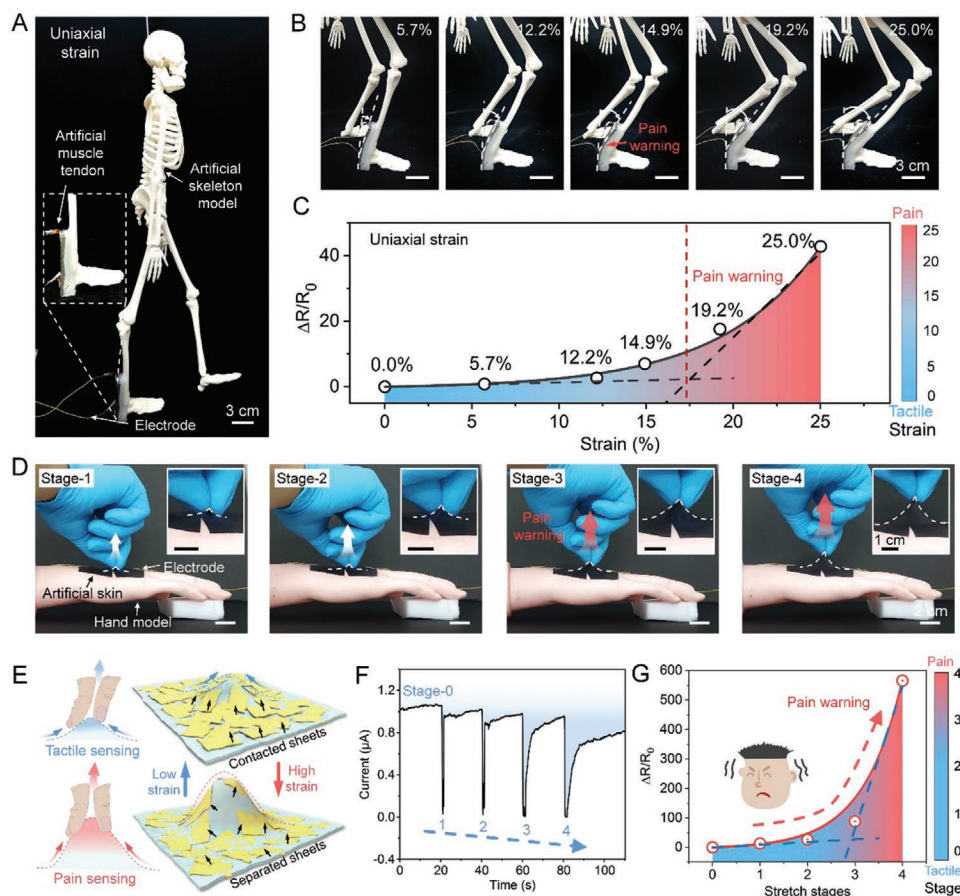


Figure 6. Soft artificial muscle tendon and skin with SPS regulation. A) Photo of ECF-based sensor transferred onto the skeleton model for an artificial muscle tendon for tactile sensing and pain warning under uniaxial strain (the sample size: $\approx 6 \times 1 \text{ cm}$). B) Photos ECF-based integrated mechanical sensor as an artificial muscle tendon for bending detection under varied uniaxial strain. C) The normalized resistance versus applied uniaxial strain with fitted color mapping, demonstrating a remarkable perception transition from tactile to pain-sensing (test number, $n = 5$). D) The ECF is integrated into a hand model surface as an artificial skin for sensing the varied stretching strain (the whole sample size: $\approx 7 \times 5 \text{ cm}$, and the circular diameter of the self-supported part: $\approx 3.8 \text{ cm}$). E) The schematic illustration of an artificial skin with tactile and pain-sensing functions. F) Current versus time curves under a series of stretch stages (test number, $n = 5$). G) The normalized resistance versus stretch stages curve with fitted color mapping, indicating a rapid increase of the normalized resistance for pain warning.

of 2 mg mL⁻¹. was carefully transferred onto the hollow hand model for a self-supported artificial skin. Moreover, mechanical force (e.g., pinch and then stretch) was successively applied to the artificial skin with varied strain. It was found that with the increase of strain, the partially embedded graphene nanosheets can experience a reversible transition from contacted state to a separated one (Figure 6E). A real-time current versus time curve was obtained, demonstrating a stepped decrease during the four stages (Figure 6F). As displayed in Figure 6G, the normalized resistance represented a sharp increase at the fourth stage with suggestive information of pain warning. The same calculated method introduced in Figure 6C was conducted to demonstrate the visual color mapping of out-of-plane strain. For this irregular deformation, the ECF could also show a typical SPS effect to regulate the specific deformation behaviors. The active perception of excessive mechanical force can provide an early warning to effectively respond to the dangers.

2.7. Biomimetic Self-Regulated Demo of Soft Perceptive Actuators

For natural creatures, stretchable skins can camouflage themselves to textured and multiple morphing forms in extreme conditions.^[35,38] Based on this phenomenon, some efforts have been dedicated to exploring multidimensional sensors. For example, superior to the conventional single axis-strain sensors, Ko et al. developed a multidimensional strain sensor to effectively differentiate strain stimuli from the principal and perpendicular directions.^[39] Interestingly, we further developed artificial skins to imitate the natural pufferfish's behavior in inflated and deflated states, which could be monitored in real time. In their systems, superior to the passive mechanical strain stiffening, the active perception of skins' strain is considered to be crucial to protect themselves from external attack and also to avoid the damage of excessive skin deformation.^[40] As shown in **Figure 7A**, some dangerous signals could trigger a living pufferfish with morphable belly to inhale air or water as a globular shape for effective defense. The sensitive capture of external stimuli and the control of 3D deformation are determined by their nerve sensory systems. Inspired by their capabilities, an artificial fish with a self-supported ECF as its belly was designed, allowing the reversible transition from 2D to 3D deformation (Figure 7B). Owing to the thin and adaptive features of ECF fabricated on water surface, the integrated fish model with a morphable artificial skin experienced a controllable actuation at low pneumatic pressure of ≈588 Pa. In a biological system, the skin can enable sensing and actuating functions, behave as a perceptive actuator to sensitively capture the danger signals and further act to regulate its deformation when exposed to a diverse environment. Also, there is a need for the attempt to respond to tiny mechanical stimuli in the design of SPS-effect-enabled skin.

For conventional sensory capability, the integrated fish model can rapidly and sensitively capture the external tiny mechanical stimuli, such as rhythmic airflow and finger touch. As shown in Figure 7C,D, a continuous and gentle non-contact mechanical stimuli of whistling was blown onto the artificial skin surface, resulting in a real-time and precise response to

the whistling signals (the response time was as low as 82 ms). In addition, mechanical stimuli in a contact mode were also conducted. When a finger touch with varied force was successively applied to the skin, it could experience a real-time response and represent a positive correlation between the normalized resistance and applied force (Figure 7E). More importantly, when the air pressure was applied, it was capable of achieving a series of 3D deformation to simulate the bulging behavior of pufferfish (Figure 7F). Furthermore, the pneumatic actuating process was effectively captured. Attributed to the introduction of SPS effect, the sensory system can dynamically transform normal tactile mode to pain warning one during mechanical deformation. Meanwhile, the normalized resistance versus pressure curve was also conducted in Figure 7G. When the pneumatic pressure was higher than the threshold value, a sharp increase of the normalized resistance could be clearly observed. Specifically, the color mapping could give a more visualized demonstration of pain warning pressure through the method in the Supporting Information. As a result, the introduction of SPS into the 3D actuating devices can further provide an integrated platform for self-regulated soft robot systems.

3. Conclusion

In this work, we have proposed SPS effect enabled soft skins, which can sensitively perceive the 2D and 3D deformation and further provide a pain-sensing warning for overstretched strain. Moreover, the SPS can be effectively regulated to a series of controllable strain thresholds to adapt to diverse conditions. As a proof of concept, the ECF integrated soft sensory systems with the SPS effect can further simulate the pain feelings of human tissues, such as the uniaxial overstretch of muscle tendons, and irregular skin deformation of pinch/stretch. More interestingly, inspired by the pufferfish, the ECF was employed to function as the self-supported artificial skin to sensitively detect the non-contact and contact mechanical stimuli and further actively monitor the real-time 3D pneumatic deformation. Also, the overinflated 3D deformation could be effectively captured by the typical SPS effect. The concept of SPS-enabled ECF is expected to provide a functional platform for achieving a warning system of 2D/3D mechanical deformation or actuation of a soft robot.

4. Experimental Section

Materials: The mechanically exfoliated graphene nanosheets with a lateral size of about 3–15 μm and thickness of ≈2.4 nm with a purity of over 90% were acquired from Ningbo Morsh Co., Ltd., which were thoroughly rinsed with anhydrous ethanol and dried in a stream of nitrogen before use. Silicon rubber (Ecoflex 00–50) was purchased from Smooth-on, USA. Prior to spray-coating, components A and B were mixed with a 1:1 weight ratio and consequently diluted using hexane with a weight ratio of 4%. General chemicals in chemical reagent grade were used as received from Sinopharm Chemical Reagent.

Preparation of Assembled Graphene Film: The ethanol-dispersed graphene nanosheets suspensions were well-dispersed using the ultrasonification method. Following a spray-coating method for appropriate volume, the uniform preassembled graphene film was formed at the air/water interface due to the Marangoni effect.

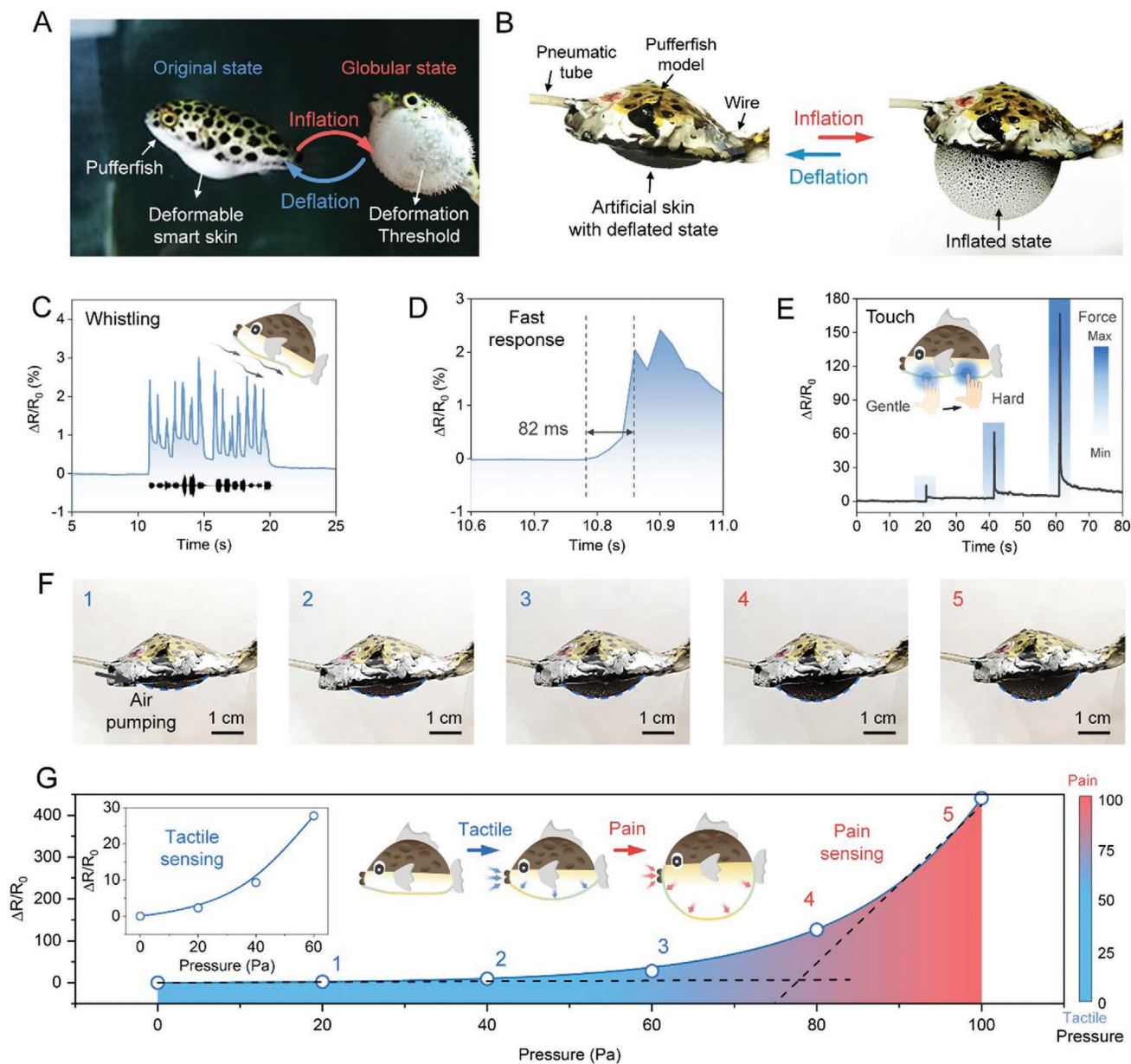


Figure 7. Artificial demo of pufferfish model for self-regulated actuation. A) Photo of pufferfish in inflated and deflated states, illustrating that it can regulate its deformation behaviors triggered by external stimuli and actively realize a mechanical deformation control via sensory systems. B) An artificial pufferfish model decorated with thin and adaptive ECF (the diameter of the self-supported film is about 2.3 cm) in a self-supported state, which can be pneumatically actuated to a similar 3D shape with a threshold control by the SPS effect. C–E) The normalized resistance versus time curves, including C) whistling capturing, D) fast response time and E) finger touch with different force, present fast and sensitive monitoring of the tiny and intense mechanical stimuli. F) Photos of artificial pufferfish model actuated by applied pressure for a series of controllable 3D deformation. G) The normalized resistance versus pressure curve with sharp improvement of the normalized resistance under unit pressure for pain warning, enabling a remarkable color mapping of pain warning (test number, $n = 6$).

Subsequently, a commercially available sponge was employed to drive the preassembled film to form a condensed structure, in which process siphon-effect induced the effective water absorption and simultaneously the homogeneous graphene preassembled layers were closely packed towards the opposite direction of the siphon direction. After several seconds, the resulted graphene film is ultimately formed with a closely packed structure. It is noted that the concentration of graphene suspension can be adjusted to 0.1, 0.5, 0.7, 1, 2, and 4 mg mL⁻¹. Further increasing the concentration of graphene may lead to poor dispersion. As a result, with the control of

concentration and sprayed volume of graphene suspension, the final thickness of assembled graphene film can be successfully adjusted.

Preparation of Graphene-Elastomer Film: The well-dissolved mixture of Ecoflex and hexane solution was carefully sprayed onto the surface of the as-prepared graphene film for a uniform layer. Note that the thickness of the ultimate elastomer layer was dependent on the sprayed volume. When the hexane solvent evaporated, a typical curing procedure (60 °C for 1 h) was achieved, resulting in a robust and homogeneous graphene-elastomer hybrid film on the water surface.

Characterization: Atomic force microscopy (AFM) images were taken by a multimode AFM (Being Nano-Instruments, Ltd) operating in the contact and/or tapping mode using silicon cantilevers (spring constant: 0.15 N m^{-1} , resonant frequency: 12 kHz for cantilever of contact mode, spring constant: $3\text{--}40 \text{ Nm}^{-1}$, resonant frequency: 75–300 kHz for cantilever of tapping mode). Field emission scanning electron microscope (FE-SEM) images were obtained with a FE scanning electron microanalyzer (Hitachi-S4800, 4 kV). Raman spectrum was collected by R-3000HR spectrometer (Raman Systems, Inc., R-3000 series) using a solid-state diode laser (532 nm) as an excitation source with a frequency range of $3000\text{--}300 \text{ cm}^{-1}$. The electrical signals were obtained by the CHI660E electrochemical system. All the human wearable sensing demonstrations based on the Janus membranes were performed at Ningbo Institute of Materials Technology and Engineering, Chinese Academy of Sciences, China. And the volunteer in Figure S7, Supporting Information was the first author of Peng Xiao that volunteered to do the demo experiment of membrane display. Furthermore, the related project was fully assessed and approved by the ethics committee of the institute with permission from all the participants.

Statistical Analysis: The experimental result of the current data was alternatively preprocessed for the normalized resistance using the normalization method. And the error bars of experimental data were presented with mean \pm standard deviation (SD). The sample size of the electrical measurement of the normalized resistance versus uniaxial strain was $5 \text{ cm} \times 5 \text{ mm}$. The software of Origin 2019 was employed to conduct one-way analysis of variance (one-way ANOVA) and the difference among samples was considered to be important when the calculated *p*-value was lower than 0.05.

Supporting Information

Supporting Information is available from the Wiley Online Library or from the author.

Acknowledgements

P.X. and W.Z. contributed equally to this work. This work was supported by the Natural Science Foundation of China (52073295), Open Research Projects of Zhejiang Lab (No. 2022MG0AB01), the Sino-German Mobility Program (M-0424), Key Research Program of Frontier Sciences, Chinese Academy of Sciences (QYZDB-SSWSLH036), Bureau of International Cooperation, Chinese Academy of Sciences (174433KYSB20170061), and K.C.Wong Education Foundation (GJTD-2019-13).

Conflict of Interest

The authors declare no conflict of interest.

Data Availability Statement

Research data are not shared.

Keywords

interlocked graphene-polymer thin-films, pneumatic soft actuation, soft skins, strain-perception-strengthening

Received: February 15, 2022
Revised: April 1, 2022
Published online: April 27, 2022

- [1] W. Yang, V. R. Sherman, B. Gludovatz, E. Schaible, P. Stewart, R. O. Ritchie, M. A. Meyers, *Nat. Commun.* **2015**, *6*, 6649.
- [2] T. Giesa, N. M. Pugno, M. J. Buehler, *Phys. Rev. E* **2012**, *86*, 041902.
- [3] E. Ducrot, Y. Chen, M. Bulters, R. P. Sijbesma, C. Creton, *Science* **2014**, *344*, 186.
- [4] Z. K. Tu, W. F. Liu, J. Wang, X. Q. Qiu, J. H. Huang, J. X. Li, H. M. Lou, *Nat. Commun.* **2021**, *12*, 2916.
- [5] K. A. Erk, K. J. Henderson, K. R. Shull, *Biomacromolecules* **2010**, *11*, 1358.
- [6] C. Storm, J. J. Pastore, F. C. MacKintosh, T. C. Lubensky, P. A. Janmey, *Nature* **2005**, *435*, 191.
- [7] M. Vatankeh-Varnosfaderani, W. F. M. Daniel, M. H. Everhart, A. A. Pandya, H. Liang, K. Matyjaszewski, A. V. Dobrynin, S. S. Sheiko, *Nature* **2017**, *549*, 497.
- [8] Y. X. Dong, A. Bazrafshan, A. Pokutta, F. Sulejmani, W. Sun, J. D. Combs, K. C. Clarke, K. Salaita, *ACS Nano* **2019**, *13*, 9918.
- [9] W. Zhang, B. Wu, S. Sun, P. Wu, *Nat. Commun.* **2021**, *12*, 4082.
- [10] M. Vatankeh-Varnosfaderani, A. N. Keith, Y. Cong, H. Liang, M. Rosenthal, M. Sztucki, C. Clair, S. Magonov, D. A. Ivanov, A. V. Dobrynin, S. S. Sheiko, *Science* **2018**, *359*, 1509.
- [11] K. M. D. Rutherford, *Anim. Welfare* **2002**, *11*, 31.
- [12] R. D. Treede, *Exp. Neurol.* **2006**, *197*, 1.
- [13] E. M. Garry, E. Jones, S. M. Fleetwood-Walker, *Brain Res. Rev.* **2004**, *46*, 216.
- [14] E. A. Lumpkin, M. J. Caterina, *Nature* **2007**, *445*, 858.
- [15] A. E. Dubin, A. Patapoutian, *J. Clin. Invest.* **2010**, *120*, 3760.
- [16] M. S. Gold, G. F. Gebhart, *Nat. Med.* **2010**, *16*, 1248.
- [17] C. J. Woolf, M. W. Salter, *Science* **2000**, *288*, 1765.
- [18] C. J. Wan, P. Q. Cai, M. Wang, Y. Qian, W. Huang, X. D. Chen, *Adv. Mater.* **2020**, *32*, 1902434.
- [19] A. Chortos, J. Liu, Z. A. Bao, *Nat. Mater.* **2016**, *15*, 937.
- [20] Q. L. Hua, J. L. Sun, H. T. Liu, R. R. Bao, R. M. Yu, J. Y. Zhai, C. F. Pan, Z. L. Wang, *Nat. Commun.* **2018**, *9*, 244.
- [21] F. L. Li, S. Gao, Y. Lu, W. Asghar, J. W. Cao, C. Hu, H. L. Yang, Y. Z. Wu, S. B. Li, J. Shang, M. Y. Liao, Y. W. Liu, R. W. Li, *Adv. Sci.* **2021**, *8*, 2004208.
- [22] B. C. K. Tee, A. Chortos, A. Berndt, A. K. Nguyen, A. Tom, A. McGuire, Z. L. C. Lin, K. Tien, W. G. Bae, H. L. Wang, P. Mei, H. H. Chou, B. X. Cui, K. Deisseroth, T. N. Ng, Z. N. Bao, *Science* **2015**, *350*, 313.
- [23] D.-H. Kim, N. Lu, R. Ma, Y.-S. Kim, R.-H. Kim, S. Wang, J. Wu, S. M. Won, H. Tao, A. Islam, K. J. Yu, T.-I. Kim, R. Chowdhury, M. Ying, L. Xu, M. Li, H.-J. Chung, H. Keum, M. McCormick, P. Liu, Y.-W. Zhang, F. G. Omenetto, Y. Huang, T. Coleman, J. A. Rogers, *Science* **2011**, *333*, 838.
- [24] P. Fratzl, N. Fratzl-Zelman, K. Klaushofer, *Biophys. J.* **1993**, *64*, 260.
- [25] D. J. Hulmes, T. J. Wess, D. J. Prockop, P. Fratzl, *Biophys. J.* **1995**, *68*, 1661.
- [26] P. Fratzl, K. Misof, I. Zizak, G. Rapp, H. Amenitsch, S. Bernstorff, *J. Struct. Biol.* **1998**, *122*, 119.
- [27] P. Xiao, J. Gu, C. Wan, S. Wang, J. He, J. Zhang, Y. Huang, S.-W. Kuo, T. Chen, *Chem. Mater.* **2016**, *28*, 7125.
- [28] S. Wang, Y. Gao, A. Wei, P. Xiao, Y. Liang, W. Lu, C. Chen, C. Zhang, G. Yang, H. Yao, T. Chen, *Nat. Commun.* **2020**, *11*, 4359.
- [29] P. Xiao, Y. Liang, J. He, L. Zhang, S. Wang, J. Gu, J. Zhang, Y. Huang, S.-W. Kuo, T. Chen, *ACS Nano* **2019**, *13*, 4368.
- [30] G. Wang, Z. Dai, Y. Wang, P. Tan, L. Liu, Z. Xu, Y. Wei, R. Huang, Z. Zhang, *Phys. Rev. Lett.* **2017**, *119*, 036101.
- [31] P. Won, J. J. Park, T. Lee, I. Ha, S. Han, M. Choi, J. Lee, S. Hong, K. J. Cho, S. H. Ko, *Nano Lett.* **2019**, *19*, 6087.
- [32] J. Jung, H. Cho, R. Yuksel, D. Kim, H. Lee, J. Kwon, P. Lee, J. Yeo, S. Hong, H. E. Unalan, S. Han, S. H. Ko, *Nanoscale* **2019**, *11*, 20356.

- [33] D. Kim, J. Bang, W. Lee, I. Ha, J. Lee, H. Eom, M. Kim, J. Park, J. Choi, J. Kwon, S. Han, H. Park, D. Lee, S. H. Ko, *J. Mater. Chem. A* **2020**, *8*, 8281.
- [34] D. Kim, J. Bang, P. Won, Y. Kim, J. Jung, J. Lee, J. Kwon, H. Lee, S. Hong, N. L. Jeon, S. Han, S. H. Ko, *Adv. Mater. Technol.* **2020**, *5*, 2000661.
- [35] J. H. Pikul, S. Li, H. Bai, R. T. Hanlon, I. Cohen, R. F. Shepherd, *Science* **2017**, *358*, 210.
- [36] P. Boyraz, G. Runge, A. Raatz, *Actuators* **2018**, *7*, 48.
- [37] H. Kim, S. K. Ahn, D. M. Mackie, J. Kwon, S. H. Kim, C. Choi, Y. H. Moon, H. B. Lee, S. H. Ko, *Mater. Today* **2020**, *41*, 243.
- [38] W. Kim, J. Byun, J.-K. Kim, W.-Y. Choi, K. Jakobsen, J. Jakobsen, D.-Y. Lee, K.-J. Cho, *Sci. Robot.* **2019**, *4*, aay3493.
- [39] K. K. Kim, S. Hong, H. M. Cho, J. Lee, Y. D. Suh, J. Ham, S. H. Ko, *Nano Lett.* **2015**, *15*, 5240.
- [40] E. L. Brainerd, *J. Morphol.* **1994**, *220*, 243.